

Supplementary information

CO₂ outperforms KOH as an activator for high-rate supercapacitors in aqueous electrolyte

Castro-Gutiérrez, J.¹, Canevesi, R. L. S.¹, Emo, M.², Izquierdo, M. T.³, Celzard, A.¹, Fierro, V.^{1,*}

¹ Université de Lorraine, CNRS, IJL, 27 Rue Philippe Séguin, 88000 Epinal, France

² Université de Lorraine, CNRS, IJL, 2 Allée André Guinier, 54011 Nancy, France

³ Instituto de Carboquímica (ICB-CSIC), Miguel Luesma Castán 4, E-50018, Zaragoza, Spain

* Corresponding author: Vanessa Fierro, vanessa.fierro@univ-lorraine.fr

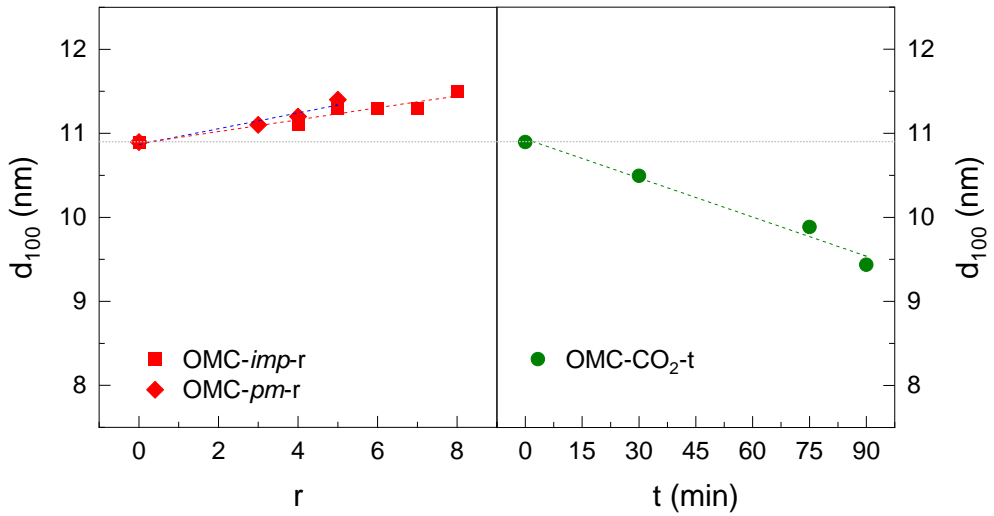


Figure S1. d_{100} interplanar spacing determined from the (100) peak of the small-angle XRD patterns for OMC-*imp*-r, OMC-*pm*-r, and OMC- CO_2 -t series of materials.

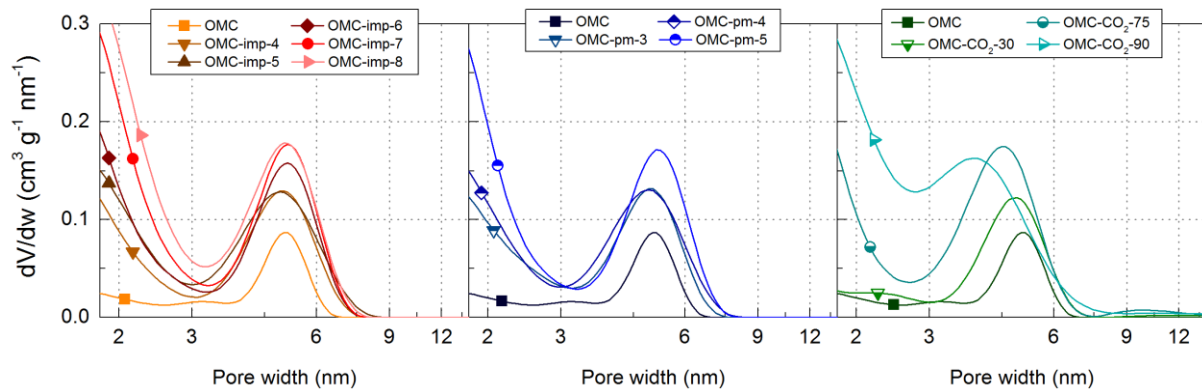


Figure S2. Differential pore size distributions in the mesopore range for the OMC-*imp*-r, OMC-*pm*-r, and OMC- CO_2 -t series of materials (Data for the OMC- CO_2 -t series are from Castro-Gutiérrez et al. (2019) [1]).

Table S1. Activation parameters and textural properties of the three series of materials compared in this study (Data for the OMC-CO₂-*t* series are from Castro-Gutiérrez et al. (2019) [1]).

Sample	Activation process	Activation time (min)	KOH/Carbon weight ratio	Burn off (%)	A_{BET} (m ² g ⁻¹)	S_{NLDFT} (m ² g ⁻¹)	V_{tot} (cm ³ g ⁻¹)	$V_{u\mu}$ (cm ³ g ⁻¹)	$V_{s\mu}$ (cm ³ g ⁻¹)	V_{meso} (cm ³ g ⁻¹)
OMC	---	---	---	---	567	847	0.38	0.16	0.07	0.16
OMC- <i>imp</i> -4	KOH – <i>imp</i>	60	4	42	1596	1551	0.89	0.21	0.35	0.33
OMC- <i>imp</i> -5	KOH – <i>imp</i>	60	5	47	1657	1540	0.96	0.15	0.41	0.40
OMC- <i>imp</i> -6	KOH – <i>imp</i>	60	6	48	1921	1768	1.07	0.20	0.46	0.40
OMC- <i>imp</i> -7	KOH – <i>imp</i>	60	7	54	2265	1940	1.25	0.17	0.60	0.49
OMC- <i>imp</i> -8	KOH – <i>imp</i>	60	8	54	2341	1940	1.34	0.14	0.62	0.57
OMC- <i>pm</i> -3	KOH – <i>pm</i>	60	3	54	1537	1511	0.87	0.16	0.07	0.16
OMC- <i>pm</i> -4	KOH – <i>pm</i>	60	4	55	1701	1613	0.96	0.20	0.33	0.34
OMC- <i>pm</i> -5	KOH – <i>pm</i>	60	5	54	2311	1992	1.26	0.20	0.38	0.38
OMC-CO ₂ -15	CO ₂	15	---	14	894	1085	0.54	0.21	0.10	0.23
OMC-CO ₂ -30	CO ₂	30	---	32	1222	1333	0.71	0.22	0.20	0.29
OMC-CO ₂ -45	CO ₂	45	---	41	1387	1416	0.80	0.22	0.26	0.33
OMC-CO ₂ -60	CO ₂	60	---	43	1479	1480	0.86	0.20	0.30	0.35
OMC-CO ₂ -75	CO ₂	75	---	59	1867	1614	1.11	0.14	0.48	0.49
OMC-CO ₂ -90	CO ₂	90	---	78	1999	1576	1.23	0.09	0.54	0.60

imp and *pm* stand for impregnation and physical mixing KOH-incorporation routes, respectively; S_{NLDFT} and A_{BET} , are specific surface areas calculated by applying 2D-NLDFT HS and BET models, respectively. Parameters calculated from the 2D-NLDFT HS PSDs: V_{tot} , total pore volume; $V_{u\mu}$, ultramicropore volume ($w < 0.7$ nm); $V_{s\mu}$, supermicropore volume ($0.7 < w < 2$ nm); $V_{meso} = V_{tot} - V_{s\mu} - V_{u\mu}$, mesopore volume ($2 < w < 50$ nm).

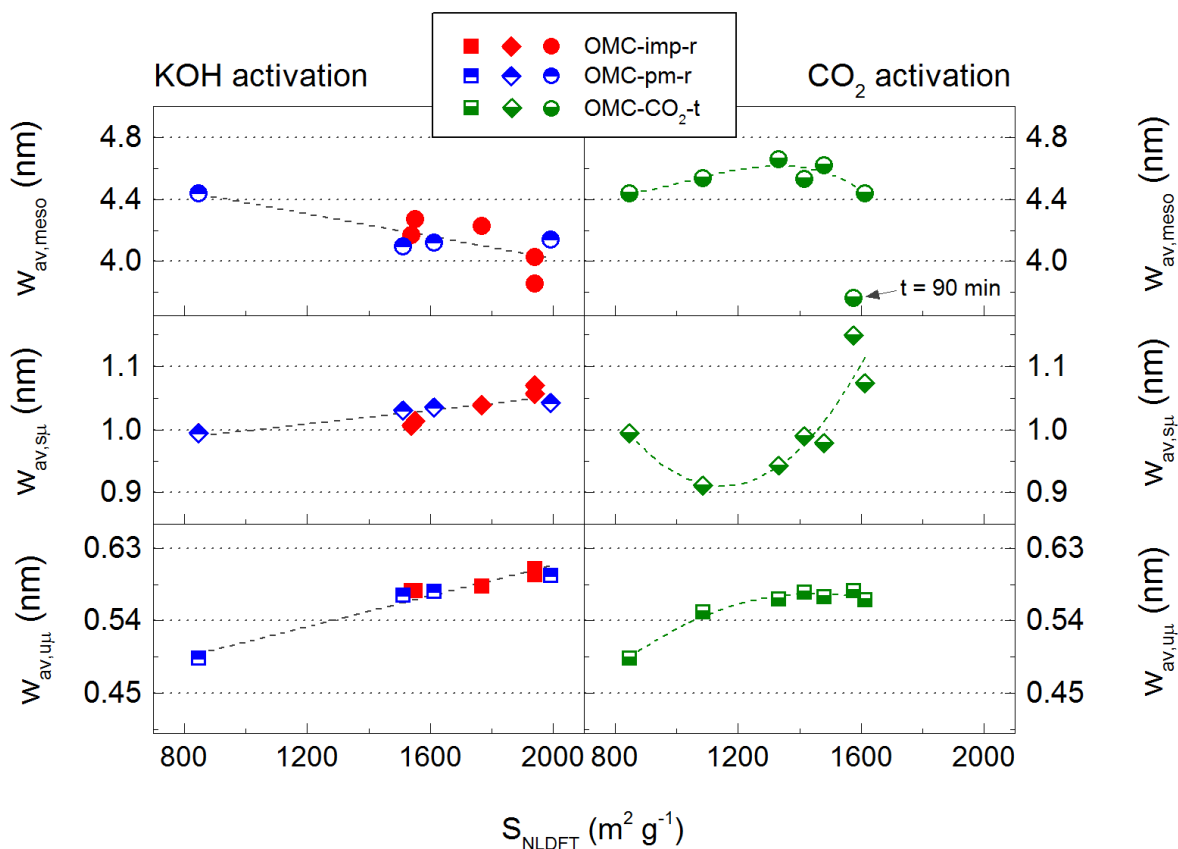


Figure S3. Average pore width as a function of S_{NLDFT} for mesopores ($w_{av,meso}$), supermicropores ($w_{av,s\mu}$) and ultramicropores ($w_{av,u\mu}$).

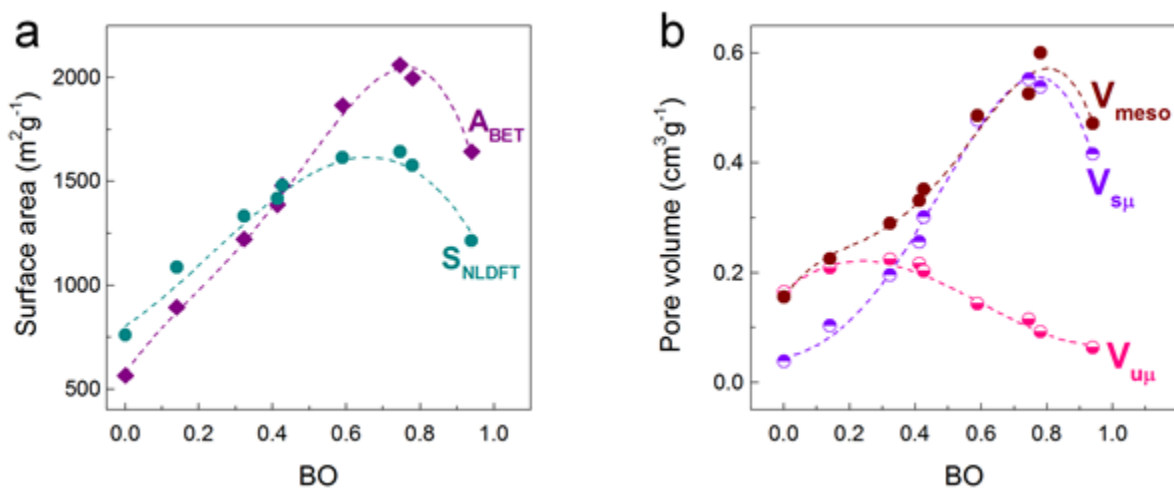


Figure S4. (a) BET area and NLDFT surface area of the OMC-CO₂-t series as a function of burn-off (BO); (b) Changes of meso-, supermicro- and ultramicropore volume (V_{meso} , $V_{s\mu}$, and $V_{u\mu}$, respectively) with BO. (Adapted with permission from Castro-Gutiérrez et al. (2019) [1]. Copyright 2019 American Chemical Society)

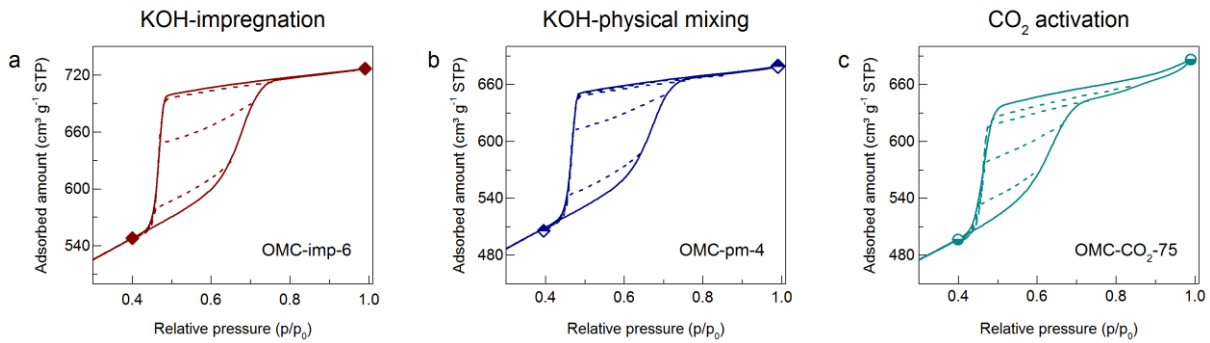


Figure S5. Scanned hysteresis loops of (a) OMC-*imp*-6, (b) OMC-*pm*-4, and (c) OMC-CO₂-75 materials activated by impregnation and physical mixing KOH-incorporation routes, and by CO₂ activation, respectively. Solid lines represent boundary adsorption and desorption curves while dashed lines represent the scanned or secondary desorption branches (Data for OMC-CO₂-75 are from Castro-Gutiérrez et al. [2]).

Table S2. Chemical composition of as-synthesized and activated materials, measured by elemental analysis (EA) and X-ray photoelectron spectroscopy (XPS) (Data for the OMC-CO₂-*t* series are from Castro-Gutiérrez et al. (2019) [1]).

Sample	EA					XPS		
	N (wt%)	C (wt%)	H (wt%)	S (wt%)	O (wt%)	C (wt%)	O (wt%)	O/S _{NLDFT} (μmol m ⁻²)
OMC	0.5	91.5	0.7	0.0	5.2	92.5	7.5	5.5
OMC- <i>imp</i> -4	0.1	95.1	0.3	0.0	3.2	95	5	2.0
OMC- <i>imp</i> -5	0.2	94.5	0.3	0.0	3.5	94.4	5.7	2.3
OMC- <i>imp</i> -6	0.2	95.0	0.2	0.0	3.1	94.1	5.9	2.1
OMC- <i>imp</i> -7	0.2	96.0	0.1	0.0	3.2	95.8	4.2	1.4
OMC- <i>imp</i> -8	0.2	96.4	0.1	0.0	2.7	96.4	3.6	1.1
OMC- <i>pm</i> -3	0.2	93.7	0.5	0.0	4.0	93.6	6.4	2.6
OMC- <i>pm</i> -4	0.2	93.9	0.4	0.0	3.7	93.7	6.3	2.4
OMC- <i>pm</i> -5	0.1	94.6	0.2	0.0	3.0	94.1	5.9	1.8
OMC-CO ₂ -15	0.3	88.8	0.9	0.0	5.9	96.0	4.0	2.3
OMC-CO ₂ -30	0.4	90.9	0.7	0.0	4.4	96.0	4.0	1.9
OMC-CO ₂ -45	0.4	91.6	0.7	0.0	4.8	95.8	4.2	1.9
OMC-CO ₂ -60	0.4	88.9	0.6	0.0	4.6	96.3	3.7	2.2
OMC-CO ₂ -75	0.6	87.2	0.5	0.0	5.1	94.8	5.2	2.5
OMC-CO ₂ -90	0.7	75.3	0.6	0.0	5.4	94.1	5.9	3.1

Table S3. Peak assignment and relative contributions of surface functionalities for as-synthesized and activated materials, calculated by deconvolution of the C1s and O1s contributions obtained by XPS analysis (Data for the OMC-CO₂-*t* series are from Castro-Gutiérrez et al. (2019) [1]).

Sample	C1s contributions					O1s contributions			
	CI	CII	CIII	CIV	CV	OI	OII	OIII	OIV
	A (BE) [% (eV)]								
OMC	68.3 (284.4)	26.9 (285.5)	3.6 (287.6)	1.2 (289.2)	---	25.6 (531.3)	67.4 (532.7)	7.0 (534.5)	---
OMC-imp-4	67.4 (284.5)	26.2 (285.5)	5.1 (287.6)	0.3 (289.1)	0.9 (290.0)	19.2 (531.7)	78.7 (533.0)	2.1 (534.5)	---
OMC-imp-5	65.9 (284.5)	26.0 (285.5)	4.1 (287.6)	0.2 (289.2)	0.3 (290.0)	5.6 (531.3)	92.8 (532.8)	1.6 (534.5)	---
OMC-imp-6	66.8 (284.5)	27.5 (285.5)	4.7 (287.6)	0.3 (289.2)	0.7 (290.0)	14.0 (531.7)	80.6 (532.9)	5.4 (534.5)	---
OMC-imp-7	64.1 (284.5)	28.2 (285.5)	5.8 (287.6)	0.4 (289.2)	1.4 (290.0)	9.7 (531.5)	84.7 (532.9)	5.6 (534.5)	---
OMC-imp-8	68.8 (284.5)	25.7 (285.5)	4.6 (287.6)	0.2 (289.2)	0.7 (290.0)	17.8 (531.4)	73.9 (532.9)	8.3 (534.5)	---
OMC-pm-3	62.4 (284.5)	28.1 (285.6)	6.8 (287.6)	0.7 (289.2)	2.0 (290.2)	11.2 (531.1)	81.1 (532.9)	7.7 (535.1)	---
OMC-pm-4	63.2 (284.5)	27.6 (285.5)	5.5 (287.6)	2.1 (289.2)	1.5 (290.4)	17.6 (531.2)	74.8 (532.9)	4.2 (534.5)	3.4 (536.8)
OMC-pm-5	61.5 (284.4)	27.4 (285.5)	6.1 (287.6)	2.1 (289.2)	2.9 (290.3)	22.2 (531.3)	66.7 (532.9)	6.6 (534.5)	4.4 (536.8)
OMC-CO ₂ -15	71.2 (284.5)	23.0 (285.5)	4.3 (287.6)	0.4 (289.2)	1.0 (290.1)	33.2 (531.1)	59.3 (532.7)	7.6 (535.1)	---
OMC-CO ₂ -30	76.3 (284.5)	21.8 (285.5)	1.9 (287.6)	---	---	35.6 (531.1)	58.4 (532.8)	5.9 (534.5)	---
OMC-CO ₂ -45	75.1 (284.5)	22.9 (285.5)	2.0 (287.6)	---	---	31.3 (531.1)	59.7 (532.7)	8.9 (534.5)	---
OMC-CO ₂ -60	75.7 (284.5)	22.2 (285.5)	2.1 (287.6)	---	---	30.1 (531.1)	60.9 (532.7)	9.0 (534.5)	---
OMC-CO ₂ -75	74.6 (284.5)	23.5 (285.5)	1.9 (287.6)	---	---	32.8 (531.1)	56.4 (532.7)	10.9 (534.5)	---
OMC-CO ₂ -90	73.9 (284.5)	24.7 (285.5)	1.4 (287.6)	---	---	26.6 (531.2)	59.7 (532.6)	11.1 (534.5)	2.6 (536.2)

A stands for the relative contribution of the functional group peak to the corresponding C1 or O1 peak. BE stands for the binding energy at which the peak is centered.

Table S4. Electrochemical performance in aqueous electrolyte (H_2SO_4) of KOH- and CO_2 -activated materials reported in the literature. Specific electrode capacitance (C_e), specific energy (E) and power (P) at 0.5 A g^{-1} . Capacitance retention (C_{ret}) was calculated by considering the capacitance at 0.5 A g^{-1} as the maximum ($C_{ret} = 100 \%$). Sample names correspond to their source names.

Sample	Precursor and description	Activating agent	A_{BET} ($\text{m}^2 \text{ g}^{-1}$)	Cell type	Carbon load ^a (mg cm^{-2})	H_2SO_4 concentration	Potential window (V)	C_e ^b (F g^{-1})	C_{ret} at 5 A g^{-1} (%)	C_{ret} at 10 A g^{-1} (%)	E / P ($\text{Wh kg}^{-1} / \text{W kg}^{-1}$)	Ref.
OMC-imp-7			2265					172	85	75	6 / 133	
OMC-pm-4	OMCs from mimosa tannin, soft-templated by mechanosynthesis	KOH	1701	2e	9.1	1 M	1	195	64	46	7 / 133	This study
OMC-pm-5			2311					195	83	75	7 / 133	
3/1	Spun fibers from phenol	KOH	1520	2e	19	2 M	--	208	82	--	--	[3]
TBC-K2.8			2417					200	83	70	5 / 110	
TBC-K3.6	Activated pine tannin-derived biochars	KOH	2554	2e	10.7	1 M	0.9	240	77	63	7 / 110	[4]
N1			1901					153	83	74	--	
N2	Commercial carbon Norit® SX2, obtained from peat and activated with steam	KOH	2400	2e	10.6	1 M	--	63	78	74	--	[5]
HG180-KOH	Activated hydrochars from α -D-glucose	KOH	2760	2e	9.5	1 M	1	270	84	80	8 / 120	[6]
AMC-6	OMC from phenol, soft-templated by EISA method	KOH	1118	3e	5	1 M		227	84	79	--	[7]
YRFC700-1:3	Yolk-shell carbon from resorcinol by low-temperature polymerization	KOH	1218	3e	2.5	2 M	1.2	397	57	53	46 / 1549 ^c	[8]
OMC-K			1475					212	82	76	--	
OMC/G-K	OMC/GO composites from phenol, soft-templated by EISA method	KOH	2109	3e	1	0.5 M	0.9	292	76	70	9 / 210	[9]
RG1			1715					469	--	55	48 ^e / --	
RG3			1652					478	--	59	61 ^e / --	
RG5	Resorcinol/GO composites obtained from sol-gel process	KOH	890	3e	1 ^d	2 M	1	433	--	62	59 ^e / --	[10]
RG10			777					480	--	46	43 ^e / --	
BRC-3	Sponge-like material from liquefied bark-phenol by thermosetting technique	KOH	2422	2e	8	1 M	1	277	68	51	10 / 234	[11]

Cell type: 2- or 3-electrode configuration, 2e or 3e, respectively

^a When a range of CL is reported, the value in this table corresponds to the average obtained from the minimum and maximum values

^b For a 2-electrode configuration, C_e was calculated considering that $C_e = 4 C_{cell}$

^c Values obtained from 2e measurements within a potential window of 1.6 V

^d Estimated CL, considering that the electrodes were prepared by dispersing 5 mg of carbon in an alcoholic solution, then drops were deposited on a glassy carbon electrode and left to dry

^e E and P values were obtained from 3e measurements

Table S5 (cont.). Electrochemical performance in aqueous electrolyte (H_2SO_4) of KOH- and CO_2 -activated materials reported in the literature. Specific electrode capacitance (C_e), specific energy (E) and power (P) at 0.5 A g^{-1} . Capacitance retention (C_{ret}) was calculated by considering the capacitance at 0.5 A g^{-1} as the maximum ($C_{ret} = 100\%$). Sample names correspond to their source names.

Sample	Precursor and description	Activation agent	A_{BET} ($\text{m}^2 \text{ g}^{-1}$)	Cell type	Carbon load ^a (mg cm^{-2})	H_2SO_4 concentration	Potential window (V)	C_e ^b (F g^{-1})	C_{ret} at 5 A g^{-1} (%)	C_{ret} at 10 A g^{-1} (%)	E / P ($\text{Wh kg}^{-1} / \text{W kg}^{-1}$)	Ref.
PAC-KOH	Activated carbon from rice straw	KOH	1909	3e	0.3	1 M	0.8	357	71	67	--	[12]
N-CCA-600	N-doped carbon capsules from pyrrole, hard-templated using silica solid-core mesoporous shells	KOH	2470	2e	--	1 M	1.1	210	84	81	9 / 134	[13]
N-CCA-700			2080					203	85	81	8 / 137	
A60-CTPW	OMCs from mimosa tannin, soft-templated by mechanochemical synthesis	CO_2	1479	2e	9.9	1 M	1	129	87	83	5 / 107	[1]
A75-CTPW			1867					147	91	89	5 / 109	
A45-DMC	Disordered mesoporous carbon from mimosa tannin, soft-templated by mechanochemical synthesis	CO_2	1819	2e	10	1 M	1	138	91	88	5 / 110	[2]
C30/30	OMC from mimosa tannin, soft-templated by phase separation	CO_2	1152	2e	15	2 M	0.8	194	76	72	4 / 118	[14]
ASC-4 h	Activated carbon material from sucrose	CO_2	2102	2e	--	1 M	0.6	142	94	90	--	[15]
CS1-6A	N-doped carbon spheres from resorcinol obtained by hydrothermal carbonization	CO_2	1224	3e	1 ^d	1 M	0.8	242	87	82	--	[16]
CS3-6A			1184					388	78	74	--	
900	Spun fibers from PAN	CO_2	376	2e	--	1 M	1	181	90	87	6 / 252	[17]
1000			705					160	90	88	6 / 225	
AC-1000	S-doped monolith from poly(divinylbenzene) obtained by sol-gel process	CO_2	2420	3e	--	2 M	1	206	86	81	--	[18]

Cell type: 2- or 3-electrode configuration, 2e or 3e, respectively

^a When a range of CL is reported, the value in this table corresponds to the average obtained from the minimum and maximum values

^b For a 2-electrode configuration, C_e was calculated considering that $C_e = 4 C_{cell}$

^c Values obtained from 2e measurements within a potential window of 1.6 V

^d Estimated CL, considering that the electrodes were prepared by dispersing 5 mg of carbon in an alcoholic solution, then drops were deposited on a glassy carbon electrode and left to dry

^e E and P values were obtained from 3e measurements

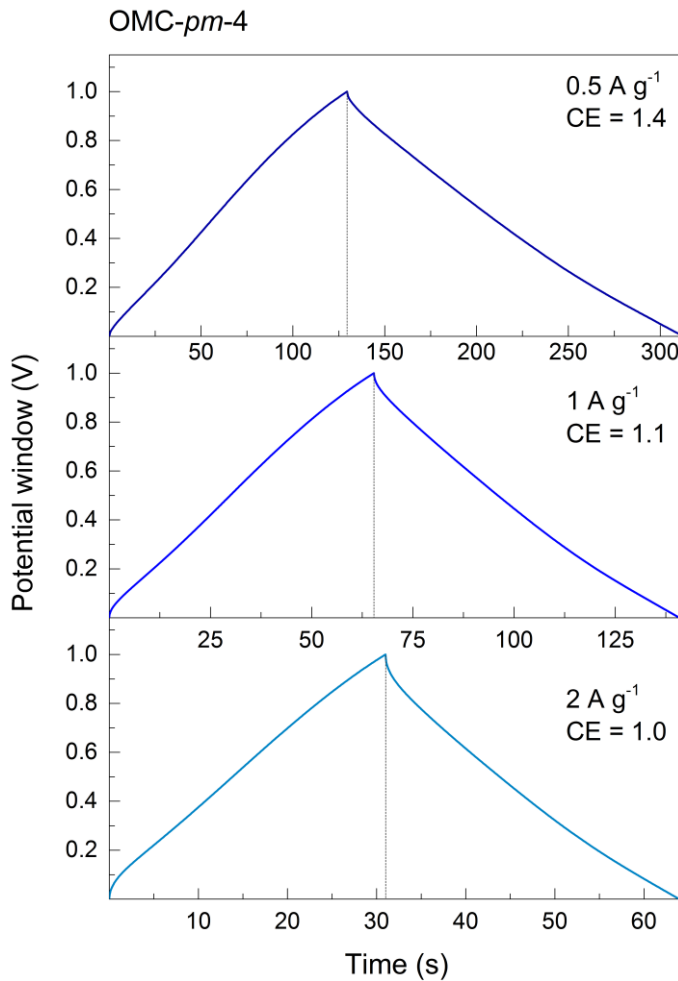


Figure S6. Charge-discharge curves for the OMC-*pm*-4 sample at different applied currents; the Coulombic efficiency (CE) is shown in each case.

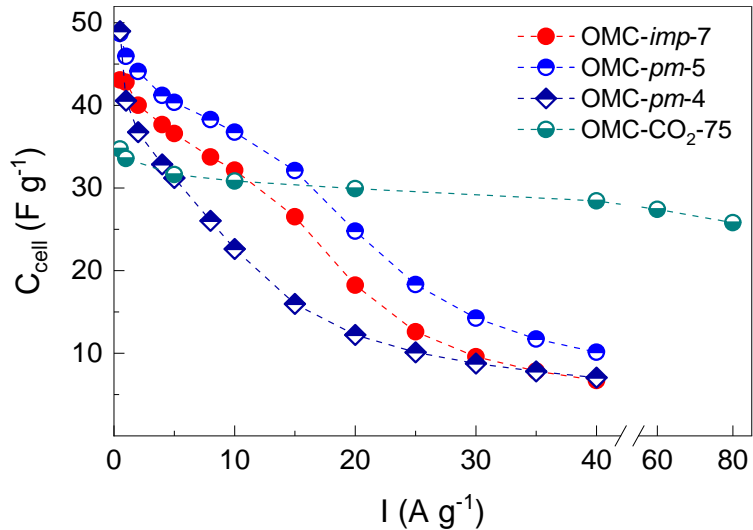


Figure S7. Specific cell capacitance (C_{cell}) as a function of specific applied current (I) for OMC-*imp*-7, OMC-pm-5, OMC-pm-4, and OMC-CO₂-75 samples (data for OMC-CO₂-75 are from Castro-Gutiérrez et al. (2019) [1]).

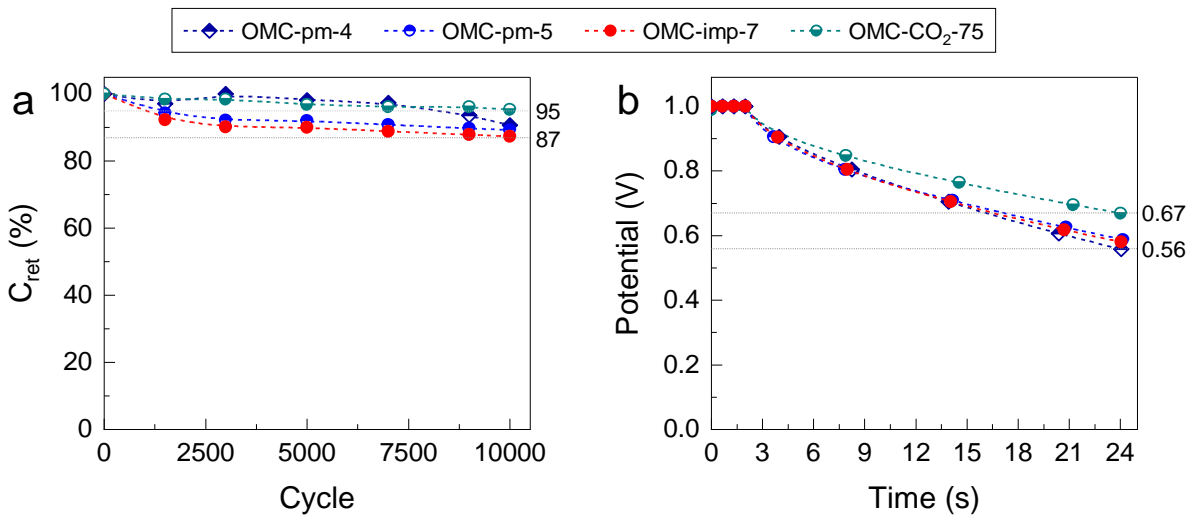


Figure S8. Long-term stability in aqueous electrolyte (1 M H₂SO₄) of tested samples: (a) capacitance retention (C_{ret}) after continuous cycling at 5 A g⁻¹; and (b) self-discharge tests.

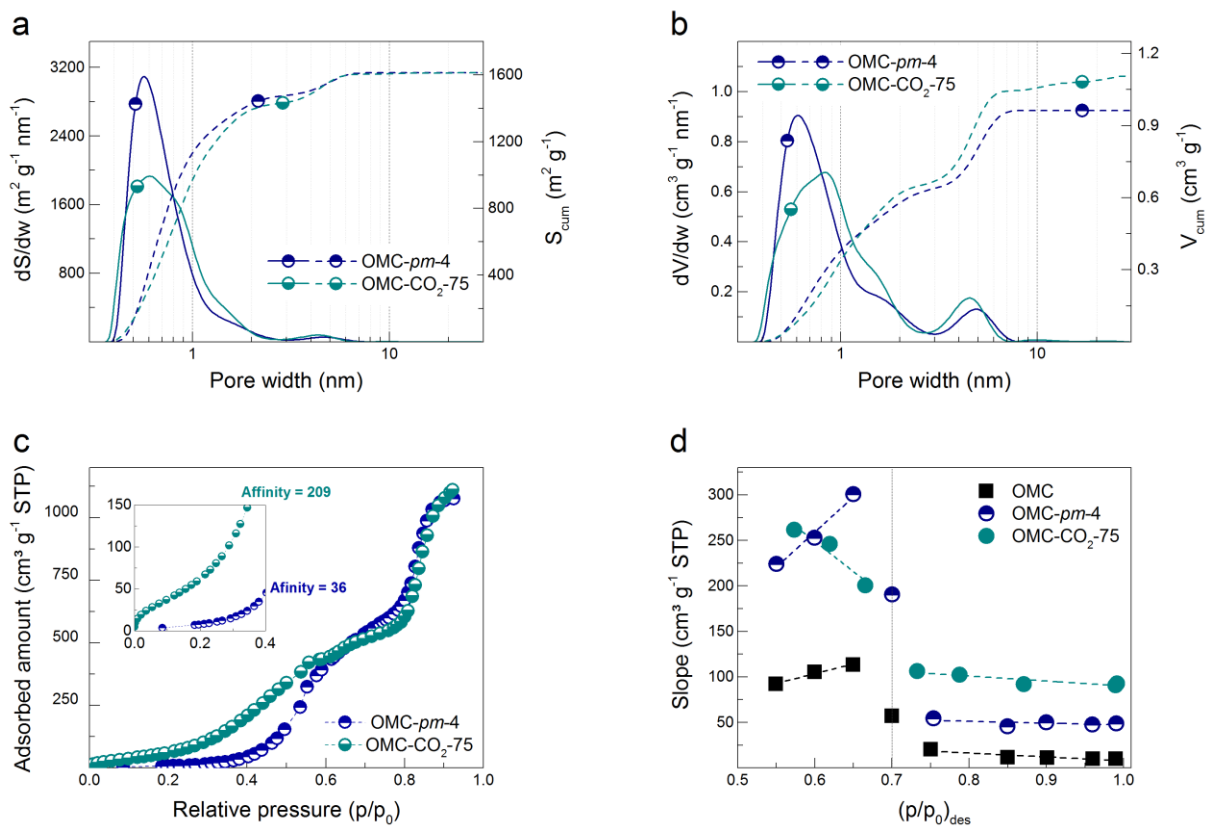


Figure S9. Comparison of OMC-pm-4 and OMC-CO₂-75 samples: differential and cumulative (a) volume and (b) surface PSDs; (c) water adsorption isotherms; and (d) slope of desorption branches as a function of relative pressure at their starting point ($p/p_0)_{des}$.

References

- [1] J. Castro-Gutiérrez, N. Díez, M. Sevilla, M.T. Izquierdo, J. Ghanbaja, A. Celzard, V. Fierro, High-Rate Capability of Supercapacitors Based on Tannin-Derived Ordered Mesoporous Carbons, *ACS Sustainable Chem. Eng.* 7 (2019) 17627–17635. <https://doi.org/10.1021/acssuschemeng.9b03407>.
- [2] J. Castro-Gutiérrez, N. Díez, M. Sevilla, M.T. Izquierdo, A. Celzard, V. Fierro, Model carbon materials derived from tannin to assess the importance of pore connectivity in supercapacitors, *Renew. Sust. Energ. Rev.* 151 (2021) 111600. <https://doi.org/10.1016/j.rser.2021.111600>.
- [3] V. Barranco, M.A. Lillo-Rodenas, A. Linares-Solano, A. Oya, F. Pico, J. Ibañez, F. Agullo-Rueda, J.M. Amarilla, J.M. Rojo, Amorphous Carbon Nanofibers and Their Activated Carbon Nanofibers as Supercapacitor Electrodes, *J. Phys. Chem. C.* 114 (2010) 10302–10307. <https://doi.org/10.1021/jp1021278>.
- [4] S. Pérez-Rodríguez, O. Pinto, M.T. Izquierdo, C. Segura, P.S. Poon, A. Celzard, J. Matos, V. Fierro, Upgrading of pine tannin biochars as electrochemical capacitor electrodes, *J. Colloid Interface Sci.* 601 (2021) 863–876. <https://doi.org/10.1016/j.jcis.2021.05.162>.
- [5] G. Lota, T.A. Centeno, E. Frackowiak, F. Stoeckli, Improvement of the structural and chemical properties of a commercial activated carbon for its application in electrochemical capacitors, *Electrochim. Acta.* 53 (2008) 2210–2216. <https://doi.org/10.1016/j.electacta.2007.09.028>.
- [6] M. Sevilla, A.B. Fuertes, A Green Approach to High-Performance Supercapacitor Electrodes: The Chemical Activation of Hydrochar with Potassium Bicarbonate, *ChemSusChem.* 9 (2016) 1880–1888. <https://doi.org/10.1002/cssc.201600426>.
- [7] Z. Wang, M. Zhou, H. Chen, J. Jiang, S. Guan, Hierarchical Activated Mesoporous Phenolic-Resin-Based Carbons for Supercapacitors, *Chem. Asian J.* 9 (2014) 2789–2797. <https://doi.org/10.1002/asia.201402338>.
- [8] M. Li, X. Chang, X. Han, W. Yin, M. Ren, Resorcinol-formaldehyde resin based porous carbon materials with yolk-shell structure for high-performance supercapacitors, *Synth. Met.* 219 (2016) 67–75. <https://doi.org/10.1016/j.synthmet.2016.05.011>.
- [9] S. Lu, Y. Song, K. Guo, X. Chen, J. Xu, L. Zhao, Effect of aqueous electrolytes on the electrochemical behaviors of ordered mesoporous carbon composites after KOH activation as supercapacitors electrodes, *J. Electroanal. Chem.* 818 (2018) 58–67. <https://doi.org/10.1016/j.jelechem.2018.04.025>.
- [10] K. Zhang, B.T. Ang, L.L. Zhang, X.S. Zhao, J. Wu, Pyrolyzed graphene oxide/resorcinol-formaldehyde resin composites as high-performance supercapacitor electrodes, *J. Mater. Chem.* 21 (2011) 2663. <https://doi.org/10.1039/c0jm02850a>.
- [11] C. Wang, T. Liu, Activated carbon materials derived from liquefied bark-phenol formaldehyde resins for high performance supercapacitors, *RSC Adv.* 6 (2016) 105540–105549. <https://doi.org/10.1039/C6RA20373F>.
- [12] Z. Chen, H. Zhuo, Y. Hu, L. Zhong, X. Peng, S. Jing, Q. Liu, X. Zhang, C. Liu, R. Sun, Self-Biotemplate Preparation of Hierarchical Porous Carbon with Rational Mesopore Ratio and High Oxygen Content for an Ultrahigh Energy-Density Supercapacitor, *ACS Sustain. Chem. Eng.* 6 (2018) 7138–7150. <https://doi.org/10.1021/acssuschemeng.8b01159>.
- [13] G.A. Ferrero, A.B. Fuertes, M. Sevilla, N-doped porous carbon capsules with tunable porosity for high-performance supercapacitors, *J. Mater. Chem. A.* 3 (2015) 2914–2923. <https://doi.org/10.1039/C4TA06022A>.
- [14] A. Sanchez-Sanchez, M.T. Izquierdo, G. Medjahdi, J. Ghanbaja, A. Celzard, V. Fierro, Ordered mesoporous carbons obtained by soft-templating of tannin in mild conditions, *Microporous Mesoporous Mater.* 270 (2018) 127–139. <https://doi.org/10.1016/j.micromeso.2018.05.017>.

- [15] L. Wei, G. Yushin, Electrical double layer capacitors with activated sucrose-derived carbon electrodes, *Carbon*. 49 (2011) 4830–1838. <https://doi.org/10.1016/j.carbon.2011.07.003>.
- [16] N.P. Wickramaratne, J. Xu, M. Wang, L. Zhu, L. Dai, M. Jaroniec, Nitrogen Enriched Porous Carbon Spheres: Attractive Materials for Supercapacitor Electrodes and CO₂ Adsorption, *Chem. Mater.* 26 (2014) 2820–2828. <https://doi.org/10.1021/cm5001895>.
- [17] E.J. Ra, E. Raymundo-Piñero, Y.H. Lee, F. Béguin, High power supercapacitors using polyacrylonitrile-based carbon nanofiber paper, *Carbon*. 47 (2009) 2984–2992. <https://doi.org/10.1016/j.carbon.2009.06.051>.
- [18] G. Hasegawa, Monolithic Electrode for Electric Double-Layer Capacitors Based on Macro/Meso/Microporous S-Containing Activated Carbon with High Surface Area, in: Studies on Porous Monolithic Materials Prepared via Sol–Gel Processes, Springer Japan, Tokyo, 2013: pp. 79–89. https://doi.org/10.1007/978-4-431-54198-1_6.